RSC Advances

ROYAL SOCIETY OF CHEMISTRY

www.rsc.org/advances

Influence of pore structures of carbon support on the surface textures of CO oxidation catalyst

Weiliang Han, Guodong Zhang, Gongxuan Lu*, Zhicheng Tang*

(National Engineering Research Center for Fine Petrochemical Intermediates, Lanzhou Institute of Chemical Physics, Chinese Academy of Sciences, Lanzhou, 730000, China)

*Corresponding author. Tel.: +86-931-4968083, Fax: +86-931-8277088, E-mail address: tangzhicheng@licp.cas.cn (Z.Tang).

Abstract

In this paper, three kinds of carbon materials, i.e., carbon sphere (non-C), microporous carbon (micro-C) and mesoporous carbon (meso-C) were synthesized. Micro-C and meso-C were prepared by adopting the microporous low silica ZSM-5 and mesoporous silica KIT-6 as templates, respectively. And Non-C was prepared by a hydrothermal route. The palladium loaded non-C, micro-C and meso-C supports were prepared by an impregnation method, and the catalysts were applied for CO oxidation. The Pd/meso-C exhibited the highest catalytic activity because meso-C supports had the well-ordered mesoporous structure, large BET surface area, porous channels and higher dispersion of Pd nanoparticle. By adjusting promoter type and content, calcined temperature, the optimal prepared conditions of catalyst were achieved: Ce loading content = 10 wt.%, calcined temperature = 200 ^{o}C. Comparing the result of characterization and activity, it was discovered that Pd-Ce/meso-C-200 catalysts had large numbers of active surface oxygen species, Ce^{3+} cationic species

and Pd^{4+} cationic species. All of these were relatively conducive to the catalytic oxidation of CO.

Keywords: Mesoporous Carbon; CO oxidation; Pd catalysts; Catalytic oxidation; Oxygen storage material

1. Introduction

Mesoporous carbon have been recognized to play an increasingly important role in heterogeneous catalysis processes as an adsorbent, catalyst support, or even catalyst on its own due to their remarkable chemical and physical properties such as large pore size, high surface area and open-framework structures, etc. Although there are numbers of synthesis methods [1-6], recently mesoporous carbon with extremely high surface areas and pore structures have been prepared by either hard or soft template methods [4-6]. Pietrzak et al. [4] synthesised mesoporous carbons, CMK-3 and CMK-8 by hard template method, the characterization results proved the presence of ordered mesoporous structure both in CMK-3 and in CMK-8. Wu et al. [6] prepared ordered 2D hexagonal mesoporous carbon/tungsten carbide (OMC/WC) composite nanomaterials by the soft-template method, the ordered mesoporous OMC/WC composites had high surface areas and large pore volumes and narrow pore size distributions. But mesoporous carbon with soft-template method possessed lower hydrothermal stability than that with hard template route, so mesoporous carbon prepared by hard template is superior method at the present.

Cerium, copper and iron are the most commonly used promoter for the Pd

catalyst in the CO low-temperature catalytic oxidation [7-12] . For example, Satauma [7] et al also investigated the effect of supports (CeO_2, TiO_2, Al_2O_3, ZrO_2, and SiO_2) on CO oxidation over Pd catalysts, which indicated that the superior oxygen storage property of CeO_2 support was one of the activity-controlling factors for CO oxidation. Deng et al [10] found that ferric-hydroxide supported Pd catalysts prepared by a co-precipitation method without calcination exhibited high activity for CO oxidation. The synergistic effect of noble metal and promoter will helpful to promote the catalytic activity.

In this paper, three kinds of different pore structure, i.e., nonporous carbon (non-C), microporous carbon (micro-C) and mesoporous carbon (meso-C) were synthesized and the effect of their structure on the catalytic performance were studied in detail. And we studied the effect of promoter type and loading content, calcination temperature on low temperature CO catalytic oxidation. Their properties were characterized by XRD, BET, TEM and XPS techniques.

2 Experimental

2.1 Synthesis of template

(1) KIT-6 synthesis

Mesoporous KIT-6 was synthesized according to the previously reported method [13]. Typically, 6.0g P123 (EO20PO70EO20, MW=5800, Aldrich) was dissolved in 217g distilled water and 11.8g 35 wt.% HCl solution with stirring at 35 ^{o}C. After the dissolution completed, 6.0g n-BuOH was added at once. Stirring for an hour, 12.9g TEOS was added to the homogeneous clear solution and the obtained mixture was left

under vigorous and constant stirring at 35 ^{o}C for 24h. Then, the solution was transferred to a Teflon-lined stainless steel autoclave at 100 ^{o}C for 24h. Finally, the product was dried at 100 ^{o}C and calcined at 550 ^{o}C for 5h to eliminate completely the template. The white mesoporous KIT-6 powder was obtained.

(2) ZSM-5 synthesis

Microporous ZSM-5 was synthesized according to our previous work [13]. The zeolites were synthesized by a one-step hydrothermal method. First, a certain amount of aluminum sulfate was mixed evenly with sulfuric acid and distilled water. This mixture was denoted as solution A. A certain amount of water glass (Na_2SiO_3) was added to distilled water, n-butylamine and seed. Then, the solution was mixed evenly and denoted as solution B. With stirring, solution A was dropped into solution B and aged at a certain temperature for a period of time, and then placed in an autoclave and crystallized for a period of time. Finally, the solution was filtered, dried and calcined to obtain ZSM-5 zeolite.

2.2 Synthesis of carbon material

In a typical synthesis of mesoporous carbon (meso-C), 2.97g of glucose was dissolved in 15ml distilled water with stirring at room temperature. After complete dissolution, 1g mesoporous silica template (KIT-6) was added. The mixture was stirred at 80 ^{o}C until a nearly dry powder had been obtained. The sample was then heated slowly to 750 °C with a ramp 1°C min^{-1} and calcined at the same temperature for 5 h to carbonize the glucose. The resulting sample was twice treated with a hot 2M NaOH solution to remove the silica template, followed by washing with water and

ethanol several times, and then drying at 60 °C. Microporous carbon (micro-C) was the same as meso-C synthesis method when ZSM-5 was used as template.

Nonporous carbon was synthetised by hydrothermal method. A glucose solution (1.0 $molL^{-1}$, 80 mL) was transferred into a stainless-steel autoclave with a 100mL capacity, and was autoclaved at 180 ^{o}C for 7 h. Then, the solution was cooled to room temperature. The black precipitate was collected and washed sequentially with water, anhydrous ethanol. Then the precipitate was dried at 80 ^{o}C for 6 h. The obtained brown solid was identified as non-C.

2.3 Catalyst preparation

Pd/non-C, Pd/micro-C and Pd/meso-C catalysts were prepared by an impregnation method. Typically, an aqueous solution of $Pd(NO_3)_2$ was added dropwise to non-carbon, micro-carbon and meso-carbon powder and impregnated for 4 h. In our previous study, when Pd loading was 1.25 wt%, the catalyst possessed superior activity of CO catalytic oxidation. So Pd loading content of all catalyst was 1.25% in this paper. The final catalysts were dried at 100 °C.

Pd-M/meso-carbon catalysts (M=Ce, Fe and Cu) were prepared by above mentioned method, only $Pd(NO_3)_3$ replaced to $Pd(NO_3)_2$ and M(NO_3)x, M(NO_3)x= $Ce(NO_3)_3$ or $Fe(NO_3)_3$ or $Cu(NO_3)_3$. The Ce loading content was 5 wt.%~15 wt.%, the calcined temperature of catalyst was 100 ^{o}C~300 ^{o}C.

2.4 Catalyst Characterization

Powder X-ray diffraction (XRD) analysis was performed to verify the crystallographic phases present in supports and catalysts. XRD patterns of the samples

were recorded on a Rigaku D/MAX-RB X-ray diffractometer with a target of Cu Kα operated at 60 kV and 55 mA with a scanning speed of 0.5 ^{o}/min. The 2θ of wide-angle ranged from 15-80^{o} and the 2θ of low-angle ranged from 0.6 to 5^{o}.

Chemical states of the atoms in the catalyst surface were investigated by X-ray photoelectron spectroscopy (XPS) on a VG ESCALAB 210 Electron Spectrometer (Mg Kα radiation; hv = 1253.6 eV). XPS data were calibrated using the binding energy of C1s (284.6 eV) as the standard.

Transmission electron microscopy (TEM) experiments were carried out to study the fine morphology of the carbon material, using a FEI TECNAIG^2 Microscope operated at 200 kV.

The specific surface area and the mean pore diameter of the catalysts were determined by nitrogen adsorption in accordance with the BET method, with a Micromeritics ASAP 2010 instrument. Prior to measurements, the samples were degassed at 150 ^{o}C for 6 h.

2.5 Measurements of catalytic performance

Catalytic activity tests were performed in a continuous-flow fixed-bed microreactor. A glass tube with an inner diameter of 6 mm was chosen as the reactor tube. About 300 mg catalyst with the average diameter of 20~40 mesh was placed into the tube. The reaction gas mixture consisting of 1 vol.% CO balanced with air was passed through the catalyst bed at a total flow rate of 50 mlmin^{-1}. A typical weigh hourly space velocity (WHSV) was 10000 mlg^{-1}h^{-1}. The composition of the influent and effluent gas was detected with an online GC-7890II gas chromatograph equipped

with a thermal conductivity detector. As we all know, CO oxidation reaction is accompanied by a reduction in the number of moles. In this paper, this change of moles was neglected. Therefore, the CO conversion rate (X_{CO}) was calculated:

$$X_{CO} = \frac{([CO]_{in}\text{vol.\%} - [CO]_{out}\text{vol.\%})}{[CO]_{in}\text{vol.\%}} \times 100 \quad (1)$$

The $[CO]_{in}$ and $[CO]_{out}$ was CO concentration (vol.%) in gas mixture before and after CO oxidation reaction, respectively. The reaction rate was calculated by X_{CO}:

$$r = \frac{N_{CO} \times X_{CO}}{W_{cat}} \quad (2)$$

The N_{CO} was CO molar flow in the reaction mixture gas ($mols^{-1}$), the W_{cat} was dosage of catalyst (g). The kinetic measurements of CO oxidation reaction at different temperature were performed in a fixed-bed quartz reactor by maintain P_{CO} and P_{O2}. The kinetic parameters were calculated according to the following equation, applied to the CO conversion:

$$r = k_{CO}P_{CO}^{x}P_{O2}^{y} \quad (3)$$

$$k_{CO} = A\exp(-Ea/RT) \quad (4)$$

$$\ln r = -Ea/RT + \ln A + x\ln P_{CO} + y\ln P_{O2} \quad (5)$$

P_{CO} and P_{O2} was CO and O_2 partial pressure in mixture gas, respectively. Ea was activation energy.

3. Results and discussion

3.1 Synthesis of carbon materials support

3.1.1 BET analysis

Fig.1A and Fig.1B show the N_2 adsorption-desorption isotherms and BJH pore

size distributions of micro-C and meso-C, respectively. According to IUPAC type of this hysteresis loops could be classified as type III in the micro-C, it was indicated that there might be a few areas of mesoporous structure. The adsorption-desorption isotherms of meso-C belonged to type IV isotherm (isotherm with hysteresis loop). Due to the capillary condensation, the adsorption branch of isotherms at higher relative pressure (more than 0.40) was inconsistent with the desorption branch, which was resulted in a hysteresis loop. And such an isotherm type indicates that shale samples contained both mesopore and a few micropore. The deduction was proved by the results of the pore size distribution measurements (see Fig.1B). The data derived from adsorption-desorption isotherms of non-C, micro-C and meso-C in Fig.1 are listed in Table 1.

Table 1 summarizes the type of promoter, BET surface areas, microporous area, external surface area, pore volumes and average pore diameters of non-C, micro-C and meso-C. In Table 1, it was found that the meso-C exhibited larger BET specific surface area and external surface area than micro-C and non-C. The BET specific surface area of non-C was same as the external surface area of non-C, which indicated the non-C was nonporous carbon material. The micro-C possessed higher microporous area than external surface area, which meant the micro-C was mainly microporous structure material. External surface area of meso-C was higher than microporous area of meso-C. Associated with the result of N_2 adsorption-desorption isotherms and BJH pore size distributions, it was conjectured that the meso-C had a large number mesoporous and a little microporous.

3.1.2 XRD analysis

Fig.2 shows the low-angle XRD patterns of the KIT-6 and meso-C. Three diffraction peaks at 0.98°, 1.65° and 1.90° appeared in Fig.2a, this illustrated that the structure of KIT-6 was an Ia3d cubic ordered mesopore. The appearance of a weak diffraction signal at 2θ was close to 1° from Fig.2b. This indicated that the structure of meso-C had a mesoporous structure, but the diffraction peaks were relatively weak, this meant that the meso-C might have a partially ordered mesoporous structure.

3.1.3 TEM analysis

The morphological properties of non-C, micro-C and meso-C are investigated by TEM and the images are shown in Fig.3. As could be seen from Fig.3a, the non-C was composed of carbon sphere. The BET results showed that non-C was nonporous structure material. However, it was clear from Fig.3b that the micro-C displayed surface agglomeration of the nanoparticles without a well-defined mesoporous structure. The results suggested that these few mesopores with a uniform size were randomly distributed among the mixture of small nanoparticles [14-15]. These mesopores were formed by the accumulation of nanoparticles. As be shown in Fig.3c, the meso-C showed ordered mesopores. The result was consistent with the low-angle XRD result.

In summary, the non-C was nonporous spherical support. The micro-C had higher microporous area than external surface area, which meant the micro-C was mainly microporous structure material. The portion of external surface area in meso-C was higher than that of microporous area, and the result of XRD and TEM indicated

that the meso-C showed ordered mesopores. All of this suggested that the meso-C was a material coexisted of a large number ordered mesoporous and a little microporous.

3.2 The effect of support on the activity of CO oxidation

The palladium loaded non-C, micro-C and meso-C supports are evaluated for the catalytic CO oxidation reaction, and the results are showing in Fig.4. As could be seen from Fig.4, the higher reaction temperature was, the better the catalytic activities was. The total conversion temperature (T_{100}) of the Pd/non-C catalyst was 125 ^{o}C. The catalytic activity of the Pd/micro-C catalyst was superior to Pd/non-C catalyst, T_{100} was 95 ^{o}C. The Pd/meso-C catalyst exhibited the highest oxidation activity, T_{100} was 90 °C for CO oxidation. Characterization results in the previous part revealed that meso-C had the largest external surface area than micro-C and non-C, and it had a well-ordered mesoporous structure. All of these were relatively conducive to the catalytic oxidation of CO. Therefore, it was the nature of the Pd/meso-C catalyst that brought about the higher catalytic activity compared to Pd/micro-C and Pd/non-C for CO oxidation. But because of the low loading amount of active component, the activity of Pd/micro-C and Pd/meso-C had a smaller gap.

Kept the constant P_{CO} and P_{O2}, the reaction rate of Pd/non-C, Pd/micro-C and Pd/meso-C catalysts at different reaction temperatures was calculated and the result was seen in Fig.5. From Fig.5, the three catalysts had different apparent activation energy, the relationship of activation energy of three catalysts was as follow: 20.30kJmol^{-1} (Pd/meso-C)> 18.49kJmol^{-1} (Pd/micro-C)> 15.84kJmol^{-1} (Pd/non-C). As we all know, the apparent activation energy increased gradually with the increase

of palladium valence state. Contrast the activity of catalyst with apparent activation energy, it was conjectured that tetravalent Pd was the main species on Pd/non-C, Pd/micro-C and Pd/meso-C catalysts.

In order to further study the activity reason of three catalysts, the Pd distribution in three samples is investigated by the TEM-EDS mapping images and the results are shown in Fig.6. It could be seen that the dispersion of Pd nanoparticles over the entire observed area of three catalysts was as follow: Pd/meso-C> Pd/micro-C> Pd/non-C. Compared with the result of Fig.1 and Table 1, the high surface area of support was beneficial to improve dispersion of Pd nanoparticle. As we all know, the high dispersion of Pd nanoparticles was one of the important factor to improve the activity of catalyst. So the Pd/meso-C catalyst exhibited the highest oxidation activity.

3.3 The effect of promoter type on the activity of CO oxidation

To improve the activity of Pd/meso-C catalyst, the promoter is introduced into the catalyst, the results is seen in Fig.7. Obviously, the addition of promoter improved helpfully the activity of Pd/meso-C catalyst. T_{100} was 70, 80 and 85 ^{o}C corresponding to the catalysts of Pd-Ce/meso-C, Pd-Fe/meso-C and Pd-Cu/meso-C catalyst, respectively. Comparing with Pd-Fe/meso-C and Pd-Cu/meso-C, Pd-Ce/meso-C catalysts had higher catalytic activity. The reason of above result is studied by XRD, XPS and TEM characterization.

Fig.8 shows the XRD patterns of Pd-Ce/meso-C, Pd-Fe/meso-C and Pd-Cu/meso-C catalysts. As we all know, the palladium species was the active composition in Pd catalyst. However, no characteristic diffraction peaks of Pd

particles appeared in all catalysts, which showed that Pd species were highly dispersed. By comparing the XRD pattern of the standard CeO_2 sample (JCPDS PDF#43-1002), the Pd-Ce/meso-C catalyst had diffraction peaks at 28.5°, 33.1°, 47.5° and 56.3° (2θ), corresponding to the (111), (200), (220) and (311) planes, respectively. Diffraction peaks at 2θ = 18.5°, 30.8°, 35.2°, 43.0°, 57.5° and 62.7° were assigned to iron hydroxide (JCPDS PDF#22-0346) and it could be observed for Fig.8(b). From Fig.8(c), the peaks at 35.5°, 38.73°, 48.7°, 58.3°, 61.5° and 66.2° was assigned to (002), (111), (-202), (202), (-113) and (-311) of CuO (JCPDS PDF#45-0937). The CeO_2, $Fe(OH)_3$ and CuO diffraction peaks existed in Pd-Ce/meso-C, Pd-Fe/meso-C and Pd-Cu/meso-C catalysts, respectively.

XPS is performed to illuminate the surface composition and the chemical state of the elements existing in these catalysts. The XPS spectra of Pd-Ce/meso-C, Pd-Fe/meso-C and Pd-Cu/meso-C catalysts are presented in Fig.9. Fig.9A showed the XPS spectra of Pd 3d for Pd-Ce/meso-C, Pd-Fe/meso-C and Pd-Cu/meso-C catalysts. From Fig.9Aa, only one peak at 337.5-337.7eV appeared, it was assigned to tetravalent Pd. However, two peaks of Pd $3d_{5/2}$ appeared at binding energies of 335.7-356.1eV and 337.5-337.7eV in Fig.9Ab and Fig.9Ac. It was indicated that there were two kinds of palladium species (bivalent Pd and tetravalent Pd) and they were coexisted on the surface of Pd-Fe/meso-C and Pd-Cu/meso-C catalysts [16]. The calculated percentages of tetravalent Pd are listed in Table 2. From Table 2, the surface Pd content order was following: Pd-Ce/meso-C> Pd-Fe/meso-C> Pd-Cu/meso-C. The portion of tetravalent Pd component in the Pd-Ce/meso-C was

higher than Pd-Fe/meso-C and Pd-Cu/meso-C. The percentages of tetravalent Pd in the Pd-Ce/meso-C, Pd-Fe/meso-C and Pd-Cu/meso-C catalysts were 1.00, 0.82 and 0.49, respectively.

Fig.9B shows the XPS spectra of O1s for the Pd-Ce/meso-C, Pd-Fe/meso-C and Pd-Cu/meso-C catalysts. In this case, three peaks (O, O′, O″) could be identified by the deconvolution of the O1s spectra. The binding energy at 529.9-530.5 eV (O) was assigned to O^{2-} in the catalysts lattice, whereas the binding energy at 532.0-532.2 eV (O′) was assigned to surface adsorbed oxygen such as O^- or OH^- [11, 17]. The binding energy about 533.5-533.8 eV (O″) was associated with adsorbed molecular water [11, 17]. Usually, a higher oxygen ad-species concentration on the catalyst surface is beneficial to the enhancement in catalytic activity [17, 18]. The relative content of the surface adsorbed oxygen species in the total surface oxygen can be estimated from the relative area of the sub-peak, the results are shown in Table 2. It could be seen that the portions of adsorption oxygen component in the Pd-Ce/meso-C and Pd-Fe/meso-C was relatively high and the value was 0.48 and 0.44, respectively. However, the percentage of O_{ads} of Pd-Cu/meso-C was only 0.34.

The morphological properties of Pd-Ce/meso-C, Pd-Fe/meso-C and Pd-Cu/meso-C catalysts are investigated by TEM and the images are shown in Fig.10. From Fig.10, the Pd nanoparticle was in form of highly dispersed clusters on Pd-Ce/meso-C, Pd-Fe/meso-C and Pd-Cu/meso-C catalysts, but the Pd nanoparticle size was different in three catalysts, the Pd-Ce/meso-C (1.23 nm) and Pd-Fe/meso-C (1.27 nm) catalysts possessed similar Pd nanoparticle size while the Pd-Cu/meso-C

catalyst owned largest Pd nanoparticle size (3.86 nm). According to the result of Fig.7, Fig.8, Fig.9, Fig.10 and Table 2, it could be seen that the adsorbed oxygen concentration of catalyst surface, the existing forms, the size and dispersion of Pd nanoparticle and surface loading content of Pd were the key factors influencing the catalytic performance of Pd-M/meso-C (M=Ce, Fe and Cu) catalysts.

Kept the constant P_{CO} and P_{O2}, the reaction rate of Pd-Ce/meso-C, Pd-Fe/meso-C and Pd-Cu/meso-C catalysts at different reaction temperatures was calculated and the result was seen in Fig.11. As can be seen from Fig.11, the apparent activation energy increased with increase surface loading of Tetravalent Pd. Compared with activity result of Pd-Ce/meso-C, Pd-Fe/meso-C and Pd-Cu/meso-C catalysts, it was discovered that the higher the apparent activation energy was, the higher the activity of catalysts was. This also indicated that tetravalent Pd was the main species on CO oxidation reaction.

3.4 The effect of promoter loading content on the activity of CO oxidation

Fig.12 shows the reaction results of CO oxidation over Pd-Ce/meso-C catalysts, which is prepared with various promoter loading contents. Obviously, Pd-Ce/meso-C catalysts exhibited high activity for CO oxidation. The reaction activity increased gradually with the increase of promoter loading content at first, and then decreased. It was observed that T_{100} were 90 ^{o}C, 70 ^{o}C, 65 ^{o}C and 70 ^{o}C for catalysts when Ce loading content were 0%, 5%, 10% and 15%, respectively. The result showed that promoter loading content was not the more the better, it had a suitable amount. If adding content of promoter was too high, the activity of catalyst would decrease

because the palladium species might be covered by the Cerium species.

3.5 The effect of calcined temperature on the activity of CO oxidation

Fig.13 shows the reaction results of CO oxidation over various Pd-Ce/meso-C catalysts which are prepared at different calcined temperature, the catalyst is marks as Pd-Ce/meso-C-x (x=calcined temperature). T_{100} were 65 ^{o}C, 55 ^{o}C and 100 ^{o}C, respectively, when the calcined temperature was 100 ^{o}C, 200 ^{o}C and 300 ^{o}C. When calcined temperature was 200 ^{o}C, the catalyst had superior activity for CO oxidation. In order to further study the effect of calcined temperature on activity of CO oxidation, all of catalysts are characterized by XRD and XPS.

Fig.14 shows the XRD patterns of Pd-Ce/meso-C-100, Pd-Ce/meso-C-200 and Pd-Ce/meso-C-300 catalysts. As the same as the result of Fig.8, no characteristic diffraction peaks of Pd particles appeared in Pd-Ce/meso-C catalysts, it was indicated that Pd species were highly dispersed. From Fig.14, the intensity of CeO_2 peaks increased with increasing of calcination temperature, and the high angle CeO_2 peaks appeared in succession. By comparing the XRD pattern of the standard CeO_2 sample (JCPDS PDF#43-1002), the diffraction peaks at 28.5^{o}, 33.1^{o}, 47.5^{o}, 56.3^{o}, 59.1^{o}, 69.4^{o}, 76.7^{o} and 79.1^{o} (2θ) appeared in Fig.14c, corresponding to the (111), (200), (220), (311), (222), (400), (331) and (420) planes, respectively. Variation of CeO_2 nanocrystal size was determined by XRD line-width broadening [19]. Respectively, the average size of crystalline CeO_2 were calculated from line broadening of the ceria (111) plane using Scherrer's formula, and the result listed in Table 3 which showed that the CeO_2 particle size sequence was Pd-Ce/meso-C-300 (11.26nm)>

Pd-Ce/meso-C-200 (6.40nm) > Pd-Ce/meso-C-100 (5.08nm).

Fig.15 shows the XPS spectra of Pd-Ce/meso-C-100, Pd-Ce/meso-C-200 and Pd-Ce/meso-C-300 catalysts. Fig.15A shows the XPS spectra of Pd 3d for Pd-Ce/meso-C-100, Pd-Ce/meso-C-200 and Pd-Ce/meso-C-300 catalysts. Only peaks of Pd $3d_{5/2}$ appeared at binding energies of 337.5-337.7eV, it was assigned to tetravalent Pd. From Table 3, The Pd loading of Pd-Ce/meso-C catalysts calcined at different temperature was as follows: Pd-Ce/meso-C-200 (0.46)> Pd-Ce/meso-C-100 (0.43)> Pd-Ce/meso-C-300 (0.37).

Fig.15B shows the XPS spectra of Ce 3d for Pd-Ce/meso-C-100, Pd-Ce/meso-C-200 and Pd-Ce/meso-C-300 catalysts. The fitting process was referred to literature [20], they (V_0, V_2, V_3, V_4, V_6, V_7) were characteristic of Ce^{4+} 3d final states and they (V_1, V_5) were characteristic of Ce^{3+} 3d final states. These phenomena showed the coexistence of Ce^{3+} and Ce^{4+} species on the surface of all four catalysts. Generally speaking, there were Ce^{3+} ions in the ceria, in order to maintain electrostatic equilibrium and will produce oxygen vacancies [13]. Namely, the formation of Ce^{3+} ions was closely associated with oxygen vacancies in ceria. Respectively, the percentages of Ce^{3+} were calculated for all four catalysts, and the result listed in Table 3. It was very clear to see that the percentage of Ce^{3+} of Pd-Ce/meso-C-200 was 0.33, which was much higher than Pd-Ce/meso-C-100 (0.21) and Pd-Ce/meso-C-300 (0.14). That was to say, there were more oxygen vacancies on the surface of Pd-Ce/meso-C-200 catalyst.

Fig.15C shows the XPS spectra of O1s for Pd-Ce/meso-C catalysts which are

prepared at different calcined temperature. As was mentioned above, three peaks at 529.9-530.5 eV (O), 532.0-532.2 eV (O′) and 533.5-533.8 eV (O″) could be identified by the deconvolution of the O1s spectra, They was assigned to O^{2-} in the catalysts lattice, surface adsorbed oxygen such as O^- or OH^- and adsorbed molecular water [11, 17], respectively. The relative content of the surface adsorbed oxygen species in the total surface oxygen can be estimated from the relative area of the sub-peak, The results are shown in Table 3. It could be seen that the portions of adsorption oxygen component in the Pd-Ce/meso-C-200 was relatively high and the value was 0.47. However, the percentage of O_{ads} of Pd-Ce/meso-C-100 and Pd-Ce/meso-C-300 was 0.32 and 0.26, respectively.

The detailed research results showed that surface area, surface adsorbed oxygen concentration, surface loading content and the existing forms of Pd were the key factors influencing the catalytic performance of Pd catalyst [21-23]. According to the characterization results, meso-C had the larger BET surface areas (Table 1), and had the special ordered pore structure (as showed by TEM). As we all known, larger surface area could expose more active facets in the oxidation reaction and a special ordered pore structure was favorable for the adsorption and diffusion of reactants and products. The palladium loaded meso-C, micro-C and non-C supports were evaluated for the catalytic CO oxidation reaction (Fig.4). So the Pd/meso-C catalyst exhibited a higher catalytic activity. The superior prepared condition of support on CO oxidation were chosen by adjusting promoter type, promoter content and calcined temperature: at 10 wt.% Ce loading content, calcined temperature was 200 ^oC, the catalyst

possessed highest activity of CO oxidation. By comparing with activity and characterization results of Pd-Ce/meso-C catalysts, the conclusions was as follows: (a) the bigger surface area of support was, the higher activity of the catalysts was; (b) tetravalent Pd was the main active species on the catalysts; (c) many Ce^{3+} species was more helpful for the formation of oxygen vacancies in catalyst surface; (d) a higher oxygen vacancies on the catalyst surface was beneficial for the enhancement in catalytic activity. It was concluded that the reaction mechanism of Pd-Ce/meso-C catalyst on CO oxidation maybe adhered to the Langmuir-Hinshelwood [24]. In other words, the adsorbed CO reacted with the surface active species oxygen, the CO were oxidized CO_2, the active oxygen species were get from reaction gas. The reaction pathway was shown in Fig.16. Because there were Ce^{3+} ions in the ceria, it would produce oxygen vacancies in order to maintain electrostatic equilibrium. O_2 of reaction gas was adsorbed in the vacancies of Ce species and CO of reaction gas was adsorbed in the Pd species. At last, activated oxygen adsorbed on Ce species reacted with CO, which was adsorbed onto Pd species, and thus the CO were oxidized CO_2.

4 Conclusions

In this paper, the meso-C and micro-C were prepared by the hard template, and the non-C was prepared by the hydrothermal method. The palladium loaded meso-C, micro-C and non-C supports were evaluated for the catalytic CO oxidation reaction. The Pd/meso-C showed relatively higher catalytic activity for CO oxidation than Pd/micro-C and Pd/non-C. The effect of catalysts prepared conditions such as promoter type and content, calcined temperature on CO oxidation were investigated in

detail. The result indicated that at 10 wt.% Ce loading content, calcined temperature was 200 ^{o}C, the catalyst possessed highest activity of CO oxidation. By comparing with activity results and characterization results of Pd-Ce/meso-C, it was discovered that the larger surface area, rich active oxygen species, more Ce^{3+} cationic species higher dispersion and smaller size of Pd nanoparticle and more Pd^{4+} cationic species were the key factors influenced the catalytic performance of Pd-Ce/meso-C catalyst.

Acknowledgements

The financial support of The National Basic Research Program of China (2013CB933201), The National Natural Science Foundation of China (21407154), The Science and Technology Program of Lanzhou city (2014-2-5) and West Light Foundation of The Chinese Academy of Sciences is gratefully acknowledged.

References

[1] M.F. Gencoglu, A. Spurri, M. Franko, J. Chen, D.K. Hensley, C.L. Heldt, D. Saha, ACS Appl. Mater. Interfaces, 6 (2014) 15068-15077.

[2] Y. Wan, Y. Shi, D. Zhao, Chem. Mater., 20 (2008) 932-945.

[3] Z. Li, M. Jaroniec, J. Am. Chem. Soc., 123 (2001) 9208-9209.

[4] J. Goscianska, A. Olejnik, R. Pietrzak, J. Taiwan. Inst. Chem. E., 45 (2014) 347-353

[5] Z. Li, G.D.D. Cul, W. Yan, C. Liang, S. Dai, J. Am. Chem. Soc., 126 (2004) 12782-12783.

[6] Y. Wang, C. He, A. Brouzgou, Y. Liang, R. Fu, D. Wu, P. Tsiakaras, S. Song, J. Power Sources, 200 (2012) 8-13.

[7] A. Satsuma, K. Osaki, M. Yanagihara, J. Ohyama, K. Shimizu, Appl. Catal. B: Environ., 132-133 (2013) 511-518.

[8] V. Abdelsayed, A. Aljarash, M.S. El-Shall, Chem. Mater., 21 (2009) 2825-2834.

[9] Y. Shen, G. Lu, Y. Guo, Y. Wang, Y. Guo, X. Gong, Catal. Today, 175 (2011) 558-567.

[10] L.Q. Liu, B.T. Qiao, Y.D. He, F. Zhou, B.Q. Yang, Y.Q. Deng, J. Catal., 294 (2012) 29-36.

[11] W. Han, Z. Tang, P. Zhang, G. Lu, RSC Adv., 4 (2014) 23262-23270.

[12] X. Yang, L. Yang, S. Lin, R. Zhou, J. Hazard. Mater., 285 (2015) 182-189.

[13] W. Han, Z. Tang, P. Zhang, G. Lu., Catal. Surv. Asia, 17 (2013) 147-155.

[14] Y. Su, Z. Tang, W. Han, P. Zhang, Y. Song, G. Lu, CrystEngComm, 16 (2014) 5189-5197.

[15] J.Y. Luo, M. Meng, X. Li, X.G. Li, Y.Q. Zha, T.D. Hu, Y.N. Xie, J. Zhang, J. Catal., 254 (2008) 310-324.

[16] K. S. Kim, A. F. Gossmann, N. Winograd., Anal. Chem., 46 (1974) 197-200.

[17] Y. Xia, H. Dai, H. Jiang, L. Zhang, J. Deng, Y. Liu, J. Hazard. Mater., 186 (2011) 84-91.

[18] W. Han, P. Zhang, X. Pan, Z. Tang, G. Lu, J. Hazard. Mater., 263 (2013) 299-306.

[19] Daniel V. Leff, Pamela C. Ohara, James R. Heath, William M. Gelbart, J. Phys.

Chem., 99 (1995) 7036-7041.

[20] M.A. Henderson, C.L. Perkins, M.H. Engelhard, S. Thevuthasan, C.H.F. Peden, Surf. Sci., 526 (2003) 1-18.

[21] F. Ying, S.J. Wang, C.T. Au, S.Y. Lai, Micropor. Mesopor. Mater., 142 (2011) 308-315.

[22] Z. Qu, F. Yu, X. Zhang, Y. Wang, J. Gao., Chem. Eng. J., 229 (2013) 522-532.

[23] Y. Xia, H. Dai, H. Jiang, L. Zhang, J. Deng, Y. Liu, J. Hazard. Mater.,186 (2011) 84-91.

[24] Z. Duan, G. Henkelman, ACS Catal., 4 (2014) 3435-3443.

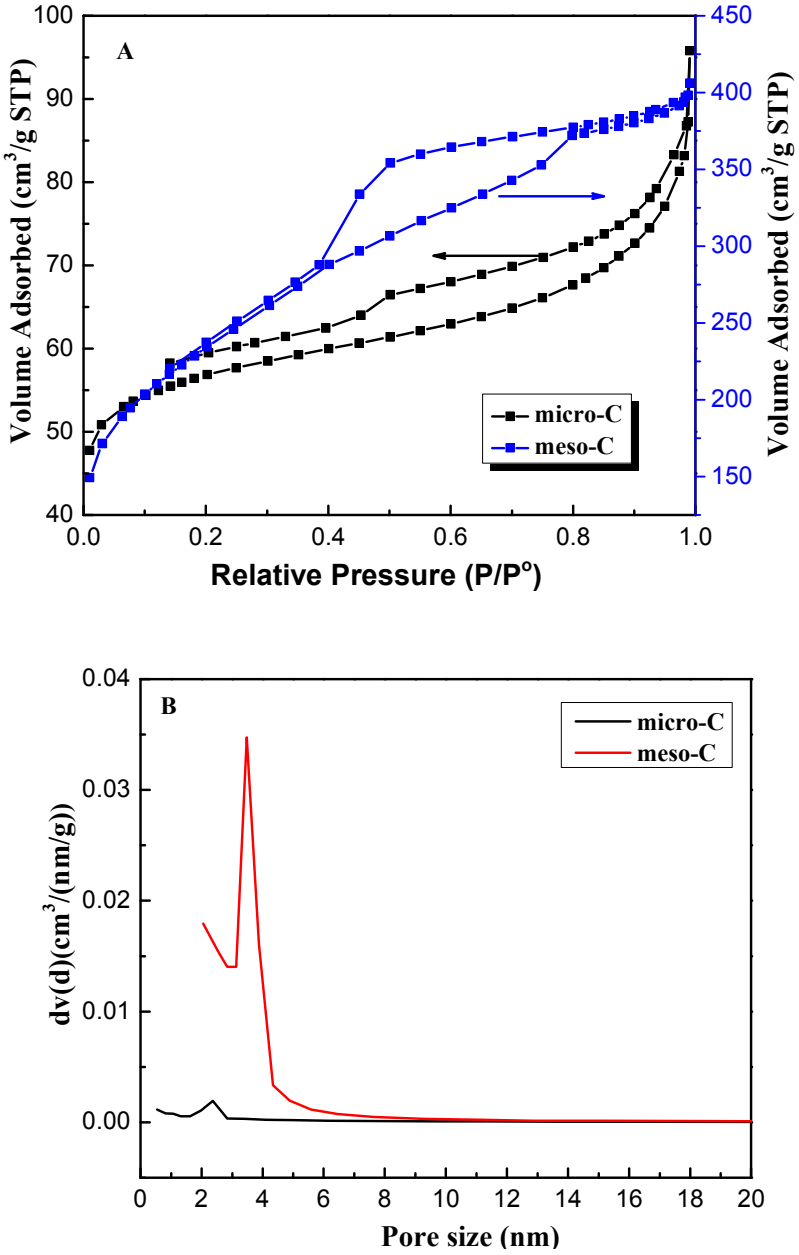

Fig.1 N_2 adsorption-desorption isotherms (A) and BJH pore size distributions (B) of meso-C and micro-C.

Table 1 Pore structure parameters of non-C, micro-C and meso-C sample

Sample	BET Surface area (m^2g^{-1})	Micropore Area (m^2g^{-1})	External surface area (m^2g^{-1})	Pore volume (cm^3g^{-1})	Average pore diameter (nm)
Non-C	6.00	0.00	6.00	-	-
Micro-C	192.28	138.39	53.89	-	-
Meso-C	833.45	163.23	670.22	0.72	3.43

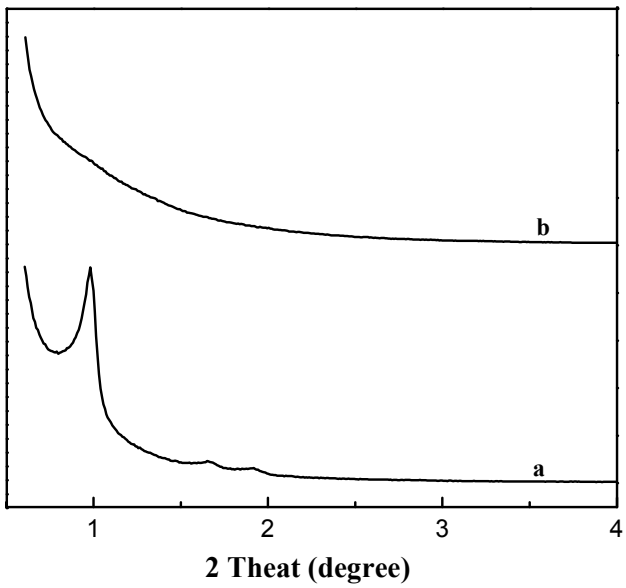

Fig.2 Low-angle XRD patterns of KIT-6 (a) and meso-C (b).

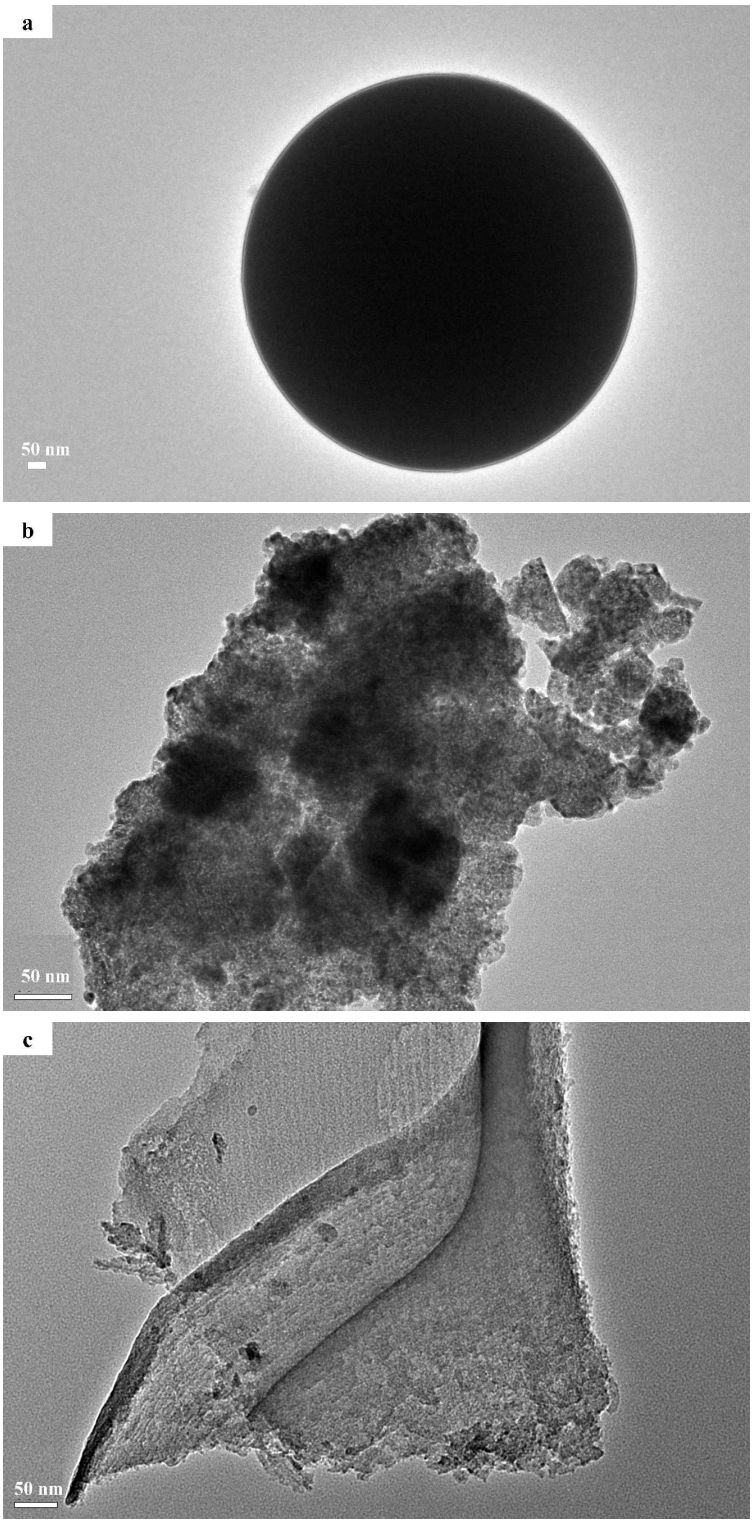

Fig.3 TEM images of non-C (a), micro-C (b), meso-C (c).

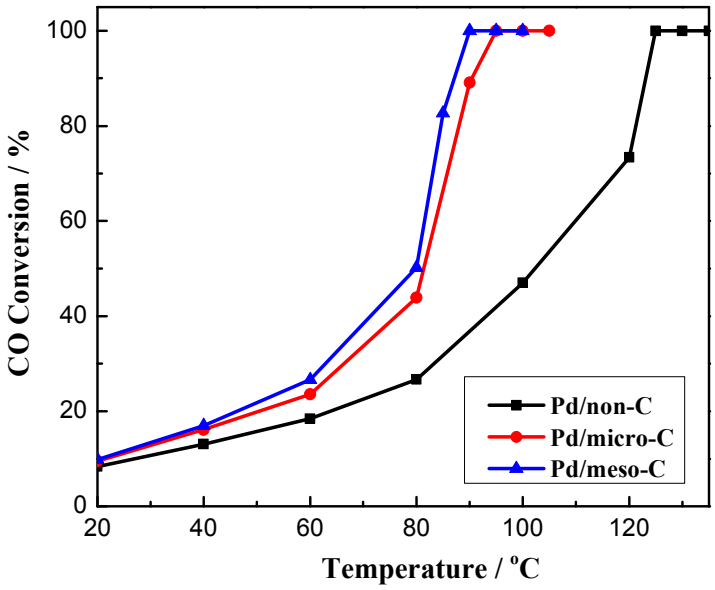

Fig.4 Catalytic activity of Pd/non-C, Pd/micro-C and Pd/meso-C catalysts for CO oxidation.

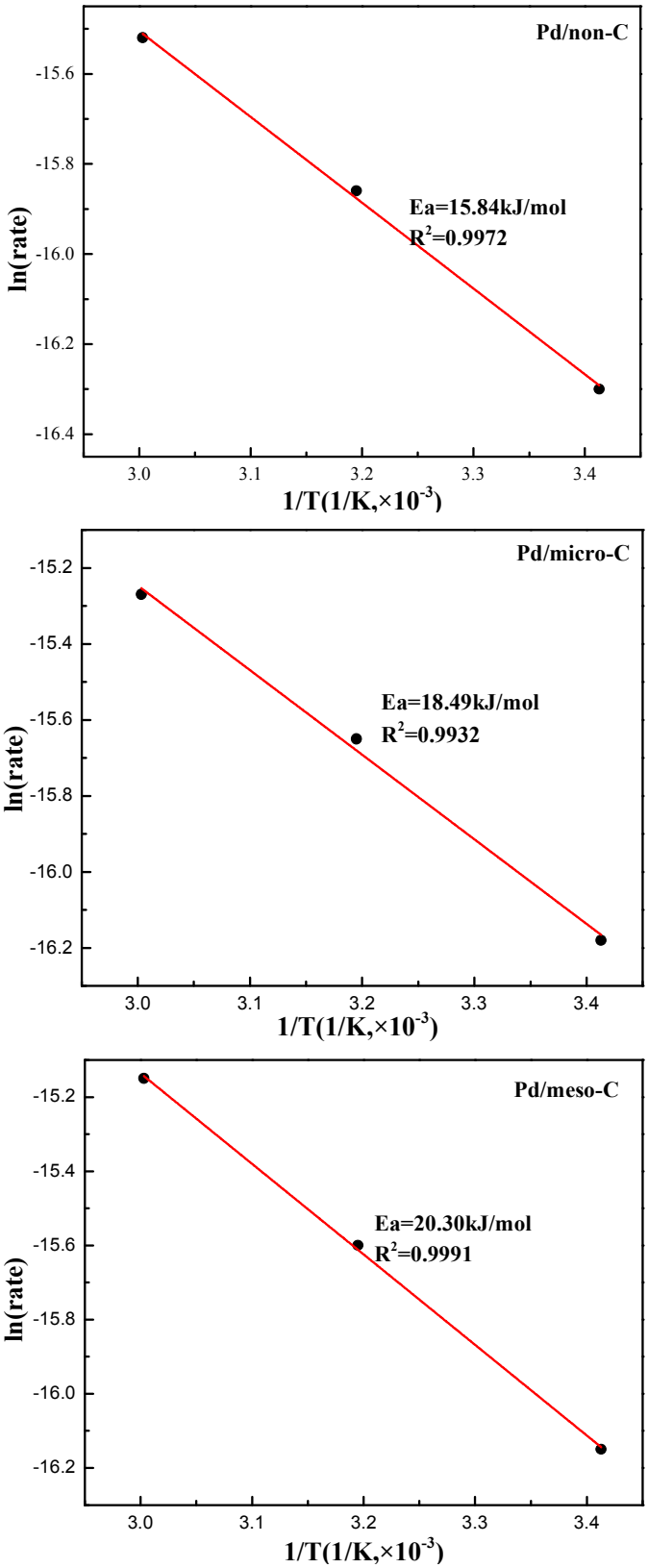

Fig.5 Arrhenius plots for CO oxidation, R^2 is correlation coefficient.

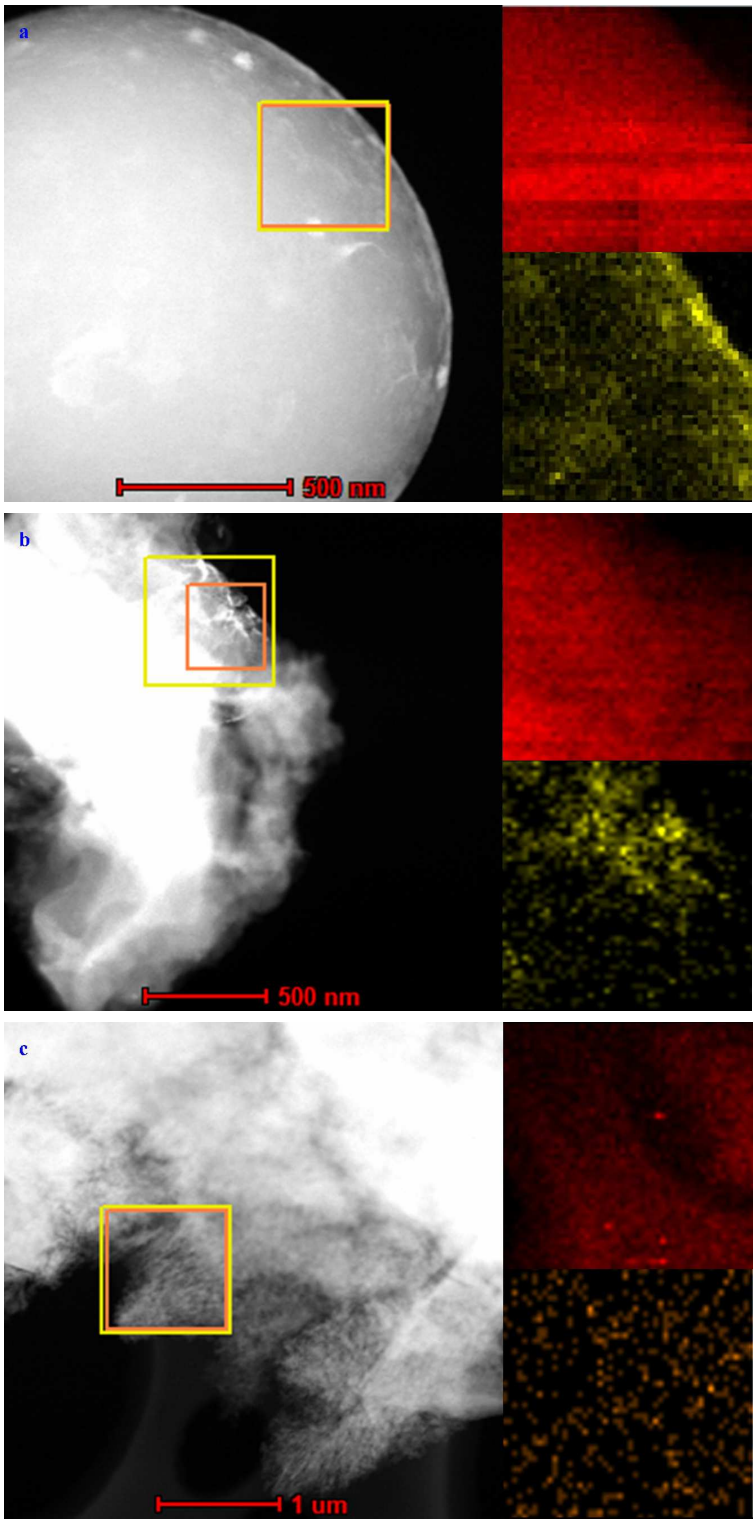

Fig.6 TEM-EDS mapping images taken from a square region in Pd/non-C (a), Pd/micro-C (b), Pd/meso-C (c) (red stands for C while another stands for Pd).

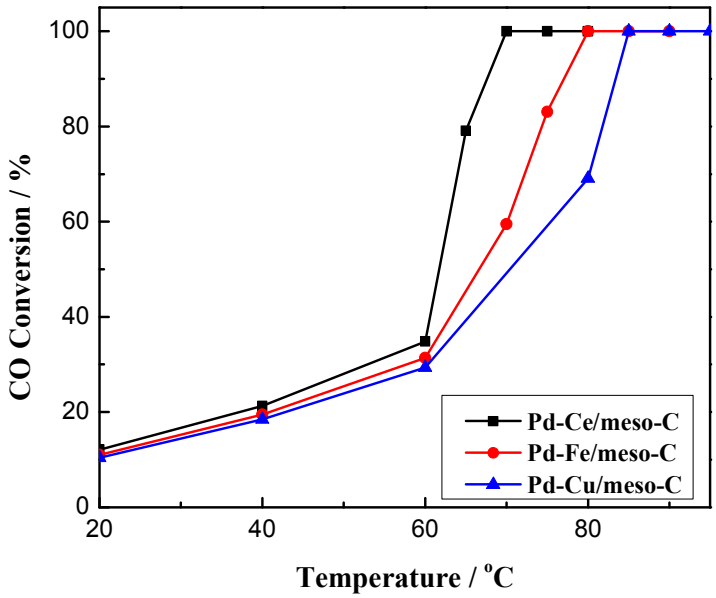

Fig.7 Catalytic activity of Pd-Ce/meso-C, Pd-Fe/meso-C and Pd-Cu/meso-C catalysts for CO oxidation.

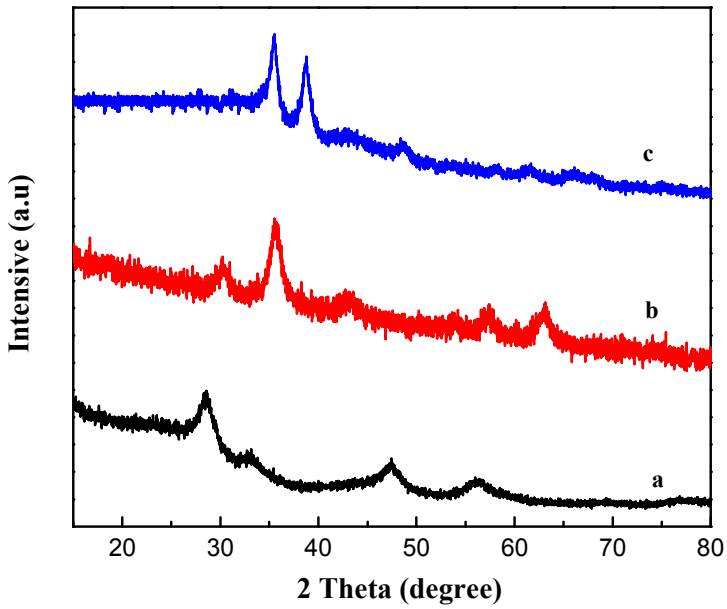

Fig.8 XRD patterns of Pd-Ce/meso-C, Pd-Fe/meso-C and Pd-Cu/meso-C catalysts.

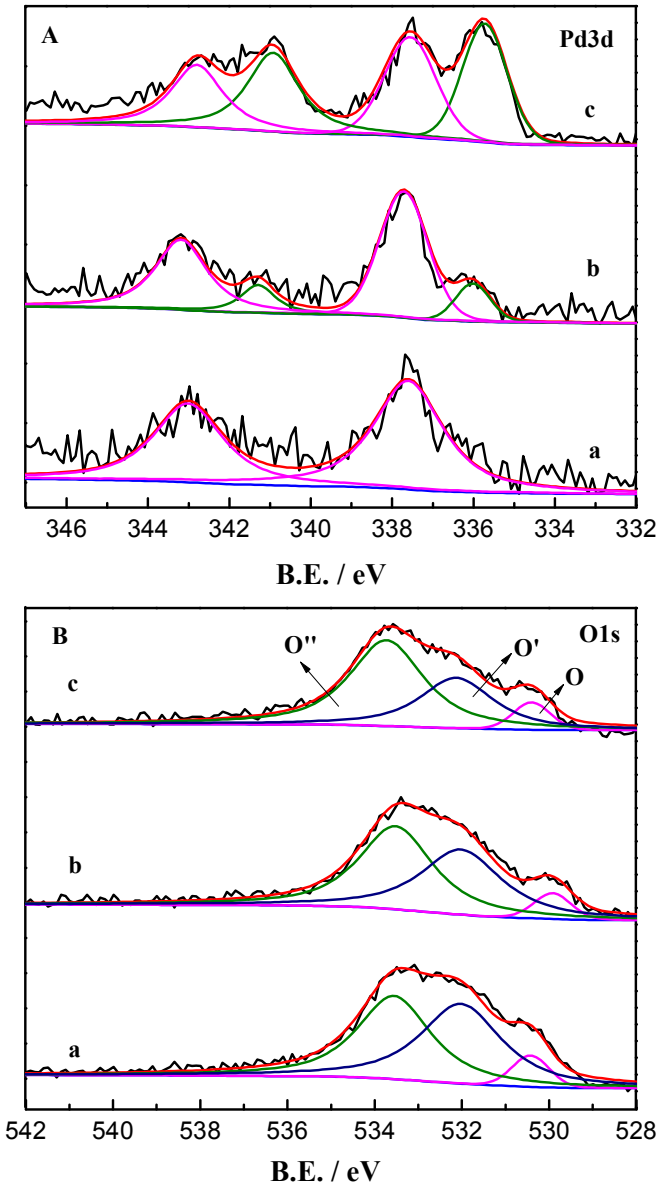

Fig.9 XPS spectra of Pd-Ce/meso-C (a), Pd-Fe/meso-C (b) and Pd-Cu/meso-C (c).

Table 2 Chemical properties of Pd-Ce/meso-C, Pd-Fe/meso-C and Pd-Cu/meso-C catalysts

Sample	$O_{ads}/(O_{ads}+ O_{latt})$	$Pd^{4+}/(Pd^{4+}+Pd^{2+})$	Pd content (%)
Pd-Ce/meso-C	0.48	1.00	0.36
Pd-Fe/meso-C	0.44	0.82	0.32
Pd-Cu/meso-C	0.34	0.49	0.26

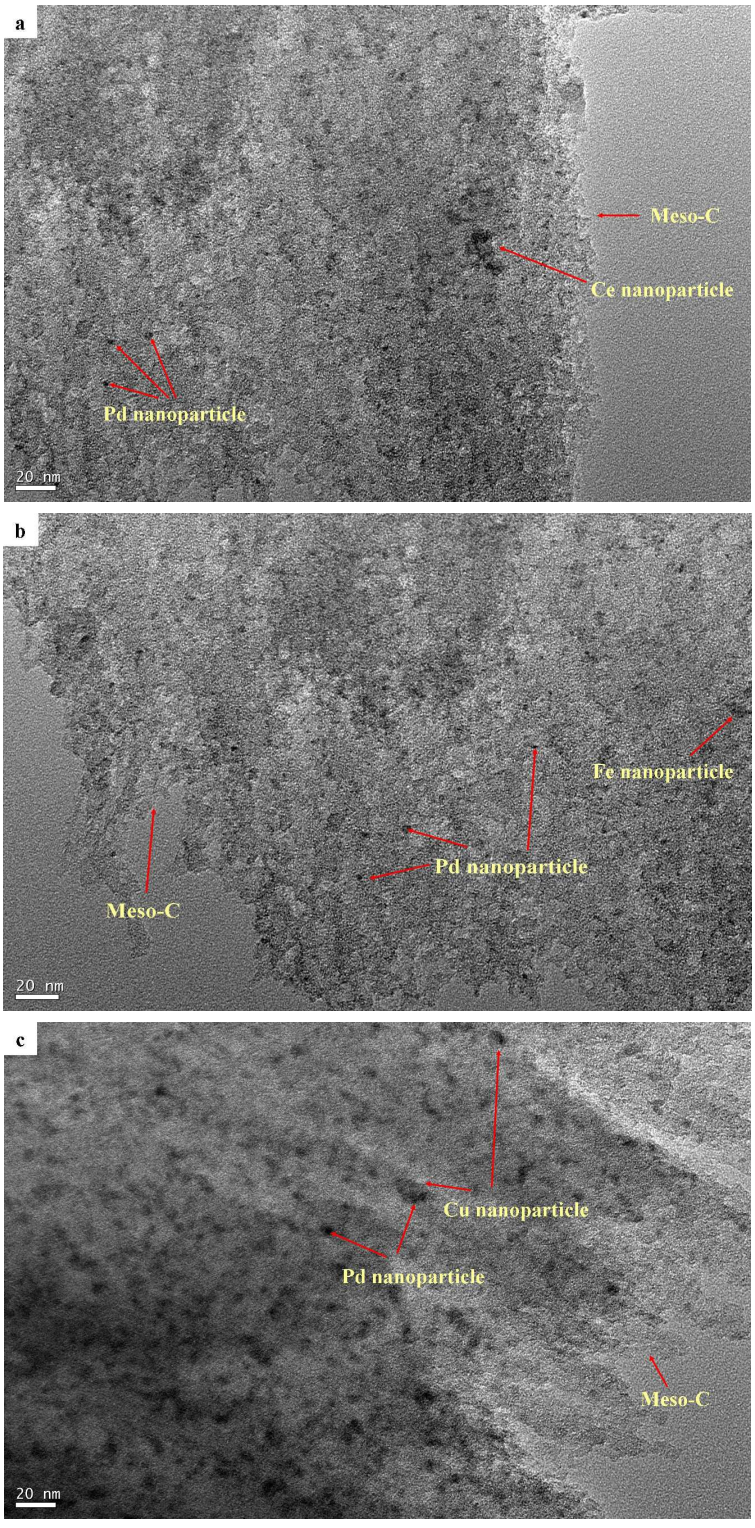

Fig.10 TEM images of Pd-Ce/meso-C (a), Pd-Fe/meso-C (b), Pd-Cu/meso-C (c).

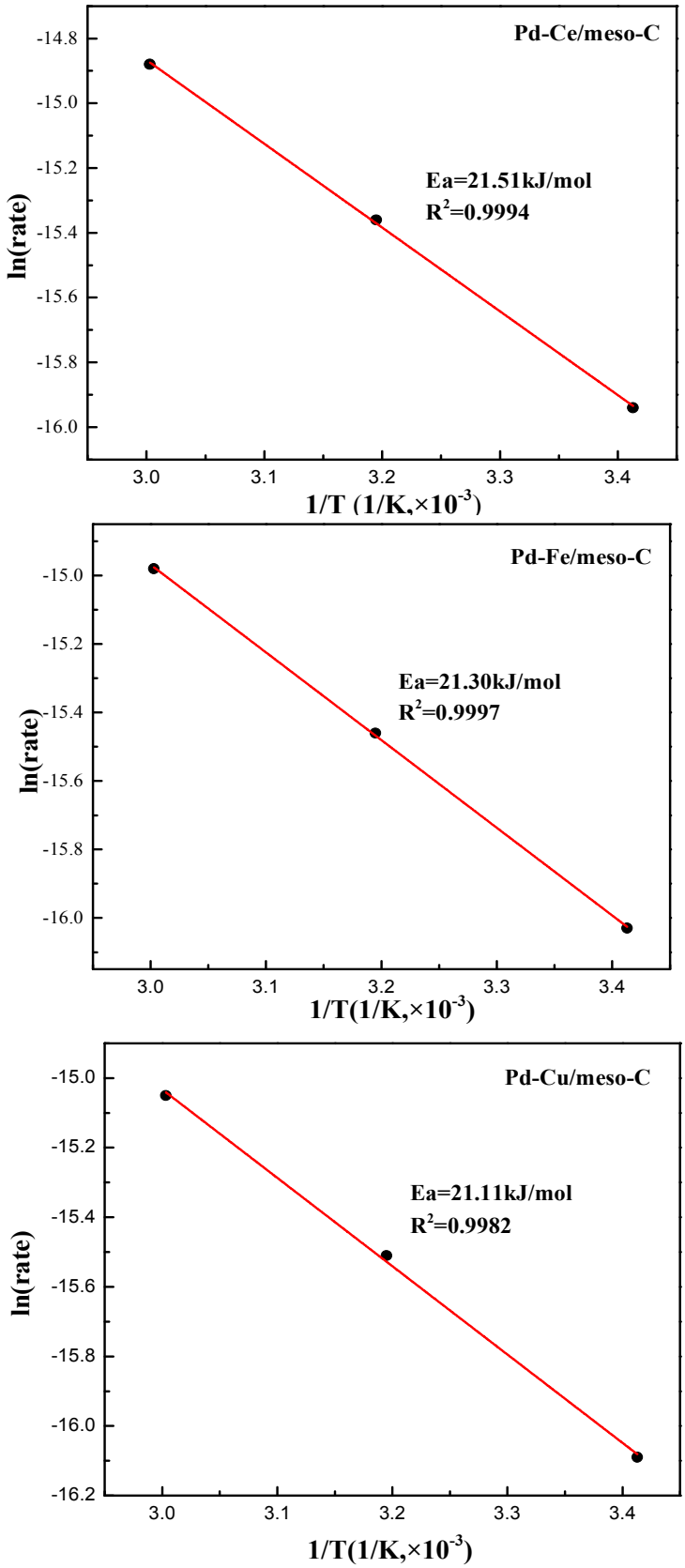

Fig.11 Arrhenius plots for CO oxidation, R^2 is correlation coefficient.

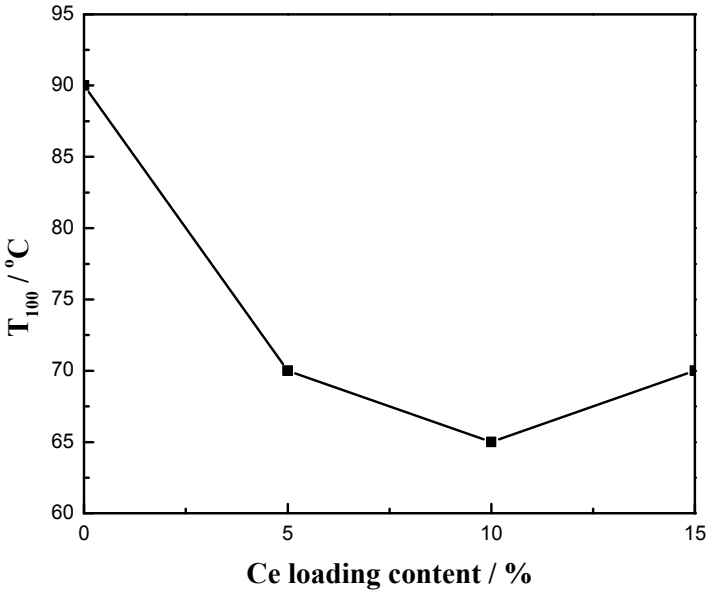

Fig.12 Catalytic activity of Pd-Ce/meso-C with different Ce loading content.

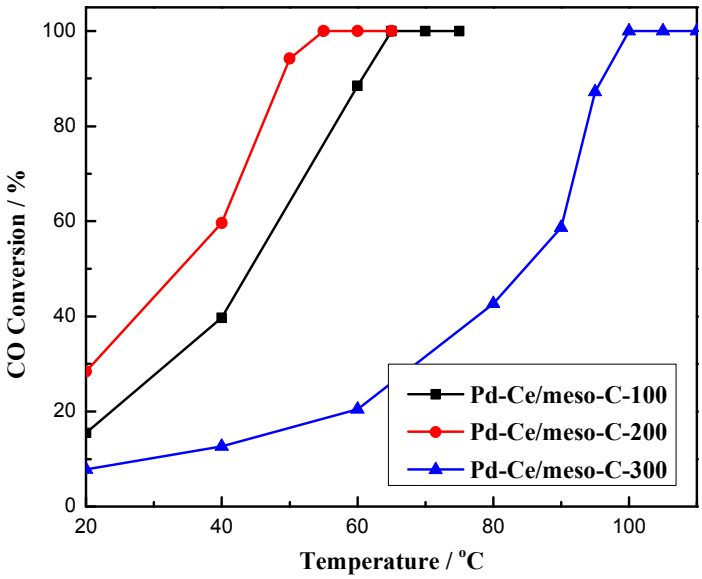

Fig.13 Catalytic activity of Pd-Ce/meso-C-100, Pd-Ce/meso-C-200 and Pd-Ce/meso-C-300.

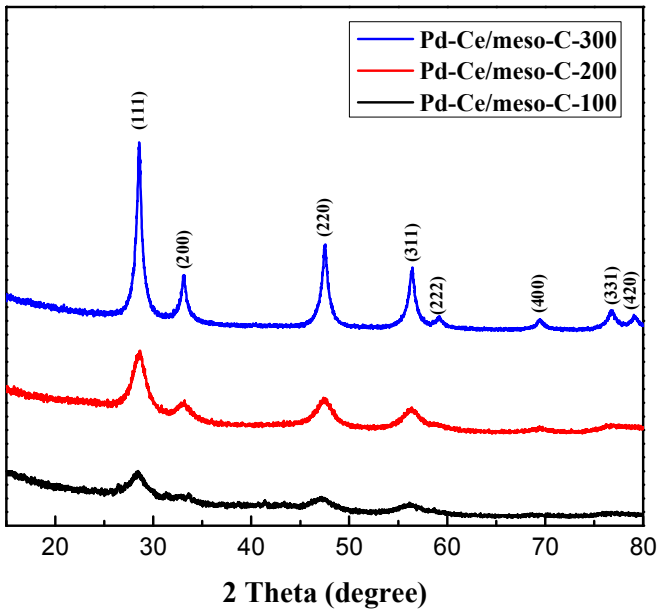

Fig.14 XRD patterns of Pd-Ce/meso-C-100, Pd-Ce/meso-C-200 and Pd-Ce/meso-C-300 catalysts.

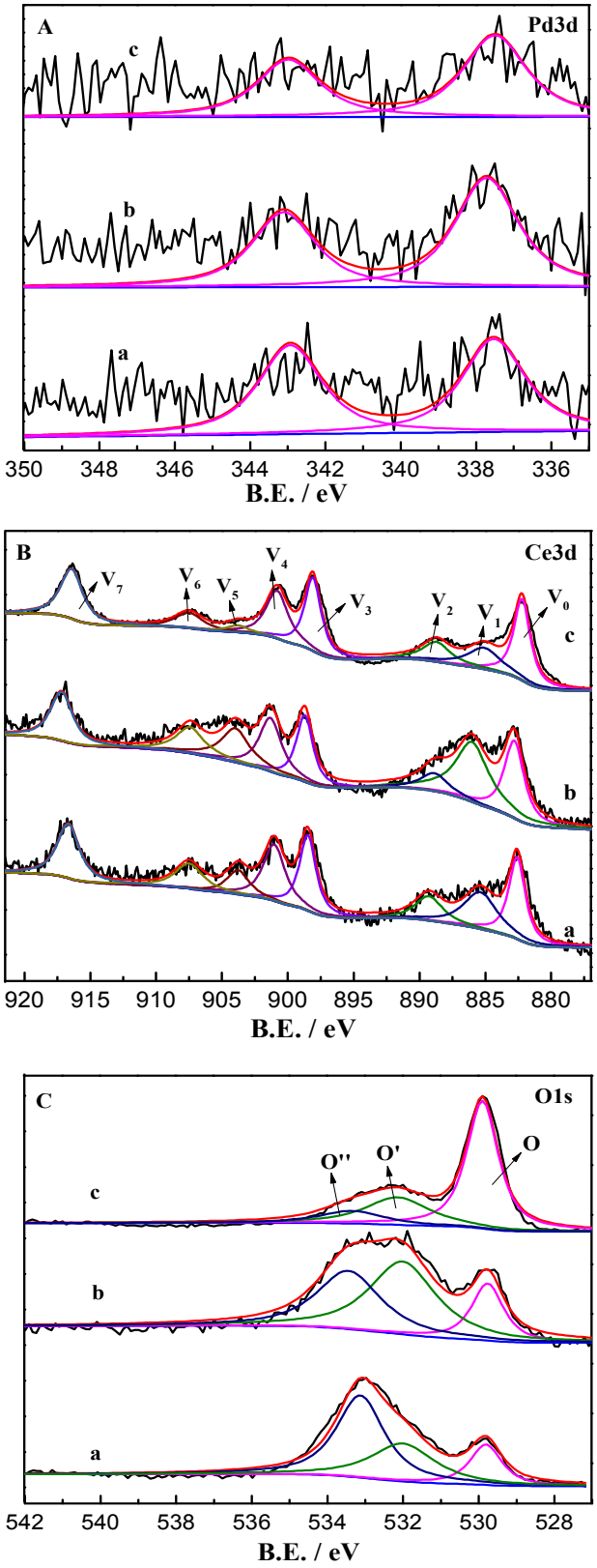

Fig.15 XPS spectra of Pd-Ce/meso-C-100, Pd-Ce/meso-C-200 and

Pd-Ce/meso-C-300 catalysts.

Table 3 Chemical properties of Pd-Ce/meso-C-100, Pd-Ce/meso-C-200 and Pd-Ce/meso-C-300 catalysts.

Sample	$Ce^{3+}/(Ce^{3+}+Ce^{4+})$	$O_{ads}/(O_{ads}+O_{latt})$	Pd content (%)	Ce content (%)	D_{CeO_2}* (nm)
Pd-Ce/meso-C-100	0.21	0.32	0.43	8.92	5.08
Pd-Ce/meso-C-200	0.33	0.47	0.46	10.22	6.40
Pd-Cu/meso-C-300	0.14	0.26	0.37	7.47	11.26

* calculated the average size of crystalline CeO_2 from line broadening of the ceria (111) plane using Scherrer's formula ($D=k\lambda/(\beta_1\cos\theta)$, k=0.943, λ=0.15405nm, $\beta_1=((\beta/180)*3.14)$, β is peak FWHM, $\theta=14.25^o$).

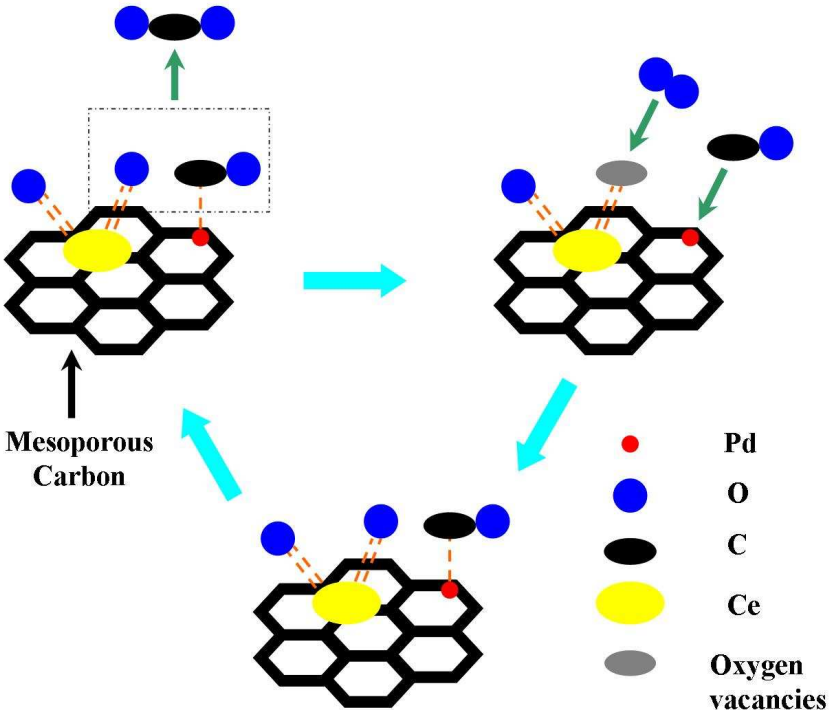

Fig.16 Reaction pathway illustration for CO oxidation over Pd-Ce/meso-C catalysts.